Received: 6 May 2024 | Revised: 22 June 2024 | Accepted: 17 July 2024

DOI: 10.1002/inf2.12617

RESEARCH ARTICLE

WILEY

Continuous synthesis of metal oxide-supported high-entropy alloy nanoparticles with remarkable durability and catalytic activity in the hydrogen reduction reaction

Wail Al Zoubi[1] | **Stefano Leoni**[2] | **Bassem Assfour**[3] | **Abdul Wahab Allaf**[3,4] | **Jee-Hyun Kang**[1] | **Young Gun Ko**[1]

[1]Intergrated Materials Chemsitry Laboratory, School of Materials Science and Engineering, Yeungnam University, Gyeongsan, Republic of Korea

[2]School of Chemistry, Cardiff University, Cardiff, UK

[3]Department of Chemistry, Atomic Energy Commission, Damascus, Syria

[4]Department of Pharmaceutical Chemistry and Quality Control, Faculty of Pharmacy, Arab International University, Darra, Syria

Correspondence
Wail Al Zoubi and Young Gun Ko, Materials Electrochemistry Laboratory, School of Materials Science and Engineering, Yeungnam University, Gyeongsan, 38541, Republic of Korea.
Email: wailalzoubi@ynu.ac.kr and younggun@ynu.ac.kr

Funding information
National Research Foundation (NRF) funded by Republic of Korea, Grant/Award Number: NRF-2022R1A2C1004392; Ministry of Science and ICT

Abstract

Metal oxide-supported multielement alloy nanoparticles are very promising as highly efficient and cost-effective catalysts with a virtually unlimited compositional space. However, controllable synthesis of ultrasmall multielement alloy nanoparticles (us-MEA-NPs) supported on porous metal oxides with a homogeneous elemental distribution and good catalytic stability during long-term operation is extremely challenging due to their oxidation and strong immiscibility. As a proof of concept that such synthesis can be realized, this work presents a general "bottom-up" l ultrasonic-assisted, simultaneous electro-oxidation–reduction-precipitation strategy for alloying dissimilar elements into single NPs on a porous support. One characteristic of this technique is uniform mixing, which results from simultaneous rapid thermal decomposition and reduction and leads to multielement liquid droplet solidification without aggregation. This process was achieved through a synergistic combination of enhanced electrochemical and plasma-chemical phenomena at the metal–electrolyte interface (electron energy of 0.3–1.38 eV at a peak temperature of 3000 K reached within seconds at a rate of ∼105 K per second) in an aqueous solution under an ultrasonic field (40 kHz). Illustrating the effectiveness of this approach, the CuAgNiFeCoRuMn@MgO-P3000 catalyst exhibited exceptional catalytic efficiency in selective hydrogenation of nitro compounds, with over 99% chemoselectivity and nearly 100% conversion within 60 s and no decrease in catalytic activity even after 40 cycles (>98% conversion in 120 s). Our results provide an effective, transferable method for rationally designing supported MEA-NP catalysts at the atomic level and pave the way for a wide variety of catalytic reactions.

KEYWORDS

activity, catalytic, metal nanoparticles, oxidation, reduction

1 | INTRODUCTION

Nanoparticles (NPs) with tunable compositions, various size, and controllable morphologies have been extensively used for energy applications and many catalytic applications[1,2]; however, to avoid synthetic complexity and prevent structural heterogeneity most NPs only contain up to three metallic elements.[1–3] Multielement alloy NPs (MEA-NPs; that is, ultrafine NPs with ≥3 elements) represent a vast and unexplored region in chemical space that could provide enhanced material tunability via a synergistic combination of various environments and different elements and high-dimensional composition control.[4–8] Compared with bare NPs, NPs anchored on porous carbon or metal oxide supports possess remarkably enhanced surface energy and specific surface area, which prevent aggregation by reducing the migration rate.[9,10] In addition, dispersion and immobilization of NPs on supports, such as carbon-based materials, metal oxides, and porous silica, zeolite, and alumina, allows further tuning of the catalyst shape, size, phase (solid solution or phase-separated) and stability, thus improving the overall catalytic activity.[3,11] Therefore, supported ultrasmall (us)-MEA-NPs (less than 10 nm) can be very useful in catalysis, energy storage, biology, and energy conversion due to their large specific surface area and abundant, single-atom active sites.[12–14]

To date, two main synthesis approaches for supported us-MEA-NPs based on tuning of the stability and collective properties have been developed: (I) in situ growth[15] and (II) synthesis-then-assembly.[16] Among the synthesis-then-assembly methods, Yao *et al*. reported a fast, high-temperature (>2000 K) process and a two-step carbothermal shock (CTS) process based on flash heating of metal salt precursors loaded onto a carbon support.[16] This process generates extremely high temperatures (∼2000 K), which arise from ultrasonic irradiation and local plasma temperatures of up to thousands of K and induce the decomposition of the loaded salt precursors to metallic NPs.[17,18] The prepared MEA-NPs can be well dispersed on carbon nanofibers via impregnation followed by electrical Joule heating (temperature of ∼3000 K) and ultrafast cooling, with a high loading rate and good size control.[19] More often, us-MEA-NPs are produced on conductive supports in situ via hydrothermal reactions or chemical reduction, which is a simple and comparatively inexpensive method[20] or sometimes via physical strategies, such as selective surface functionalization[21] and in situ electron-beam radiation.[22] As-prepared us-MEA-NPs tend to redistribute and agglomerate during synthesis and after heat treatment since the interactions between us-MEA-NPs and support materials are weak and because conductive materials are nonwetting for most metals, leading to performance deterioration following us-MEA-NP agglomeration and/or detachment.[23,24] Previous methods were carried out at high temperature to yield a favorable Gibbs free energy ($\Delta G_{mix} = \Delta H_{mix} - T^*\Delta S_{mix}$) and a high-entropy environment for the synthesis of us-MEA-NPs.[25] A small mixing enthalpy (ΔH_{mix}) is essential for promoting the formation of us-MEA-NPs; therefore, the produced particles are generally larger than 10 nm because high temperatures increase particle growth and atomic diffusion. Similar conclusions were reported in many earlier studies; for example, Yang *et al.* constrained the mixing enthalpy to $\Delta H_{mix} < 5$ kJ mol^{-1} by applying with empirical single-phase selection rules, and Stocks *et al.* reported that a small $\Delta H_{mix} < 3.57$ kJ mol^{-1} was a safe upper limit for single-phase alloys.[26] Thus, mixing strongly repulsive transition metals with an intrinsically high ΔH_{mix} (e.g., Cu-Mo with a ΔH_{mix} of 19 kJ mol^{-1}, Mo-Sn with a ΔH_{mix} of 20 kJ mol^{-1}, and Au-W with a ΔH_{mix} of 12 kJ mol^{-1}) is highly challenging. Hu *et al.* described a high-entropy and high-temperature-based method (in which MEA-NPs were produced under a high $T^*\Delta S_{mix}$ at 1800 K) to overcome the immiscibility of strongly repulsive combinations (e.g., Mo-Cu, Au-W, and Mo-Sn), which increases the range of possible transition metal alloys that can be mixed.[27] A high temperature places greater demand on the equipment and causes agglomeration of atoms, resulting in a decrease in the surface area and the number of active sites.[28] Thus, novel approaches that are transferable and potentially universal must be developed to further broaden the compositions range of metallic NPs and enhance their catalytic properties. Among the core challenges, overcoming the immiscibility of transition metals with high mixing enthalpies is paramount for realizing single-phase solid solutions at local high temperatures.

In general, the synthesis strategies for supported us-MEA-NP catalysts and the chemical nature of the support materials, whether metal oxides (e.g., Al_2O_3, TiO_2, SiO_2, or ZrO_2) or nanooxides (e.g., graphite and SiC), play important roles in controlling the final properties of the NPs. Very strong metal support interactions (SMSIs) between support materials and oxide NPs generally hamper chemical reduction of NPs.[28] For instance, Co_3O_4-based catalysts with nonreducible supports such as Al_2O_3 and SiO_2 prepared via conventional impregnation with nitrate precursor aqueous solutions were difficult to reduce to metallic Co in a H_2 atmosphere, resulting in conitration after calcination. Additionally, although reduction of Co_3O_4 on a reducible support is thermally feasible, it is more difficult than reduction of unsupported Co_3O_4.

Herein, we report a straightforward, transferable and general strategy based on ultrasonic-assisted simultaneous electro-oxidation–reduction-precipitation (U-SEO-P) to

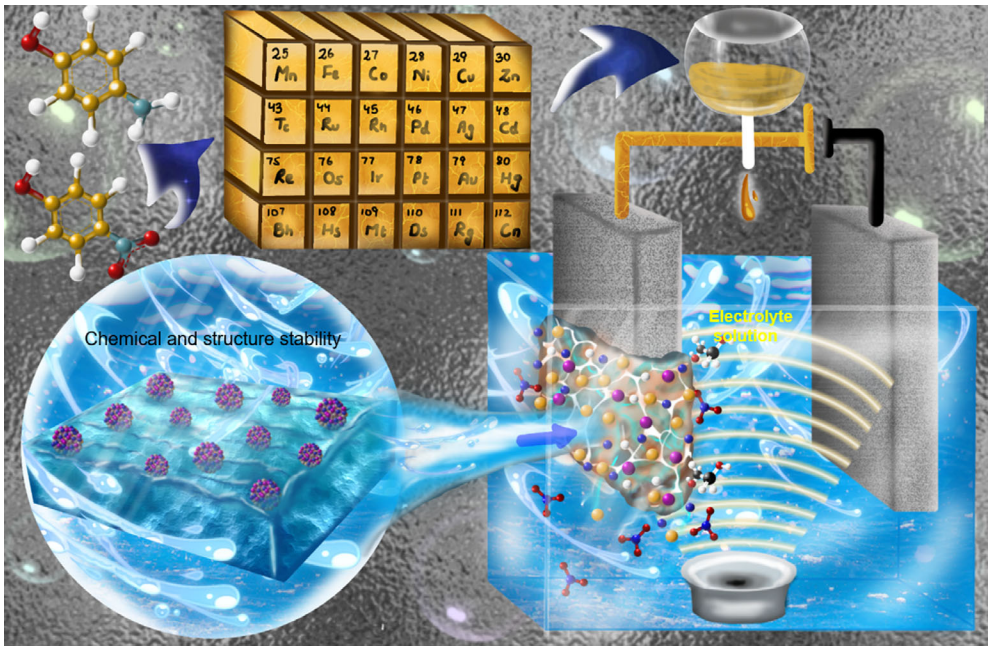

SCHEME 1 Schematic illustration of us-MEA-NP@MgO-P3000 fabrication with the U-SEO-P synthetic approach.

synthesize stable us-MEA-NPs supported on porous metal oxide substrates (Scheme 1). The resulting CuCoNi-, CuAgCoNiFe-, and CuAgNiFeCoRuMn-NPs (down to 4 nm in size, which are the smallest MEA-NPs reported thus far) were firmly anchored and well dispersed on magnesium oxide (MgO-P3000, i.e., formed via plasma discharge at 3000 K), which played a critical role in stabilizing the us-MEA-NPs. Compared to direct support on conductive materials such as carbon,[25] the MEA-NPs showed better chemical stability when dispersed on defective MgO-P3000. Density functional theory (DFT) calculations revealed that the binding energy of CuAgNiFeCoRuMn-NPs dispersed on defective MgO-P3000 was much greater than that on defective carbon, suggesting better overall stability of CuAgNiFeCoRuMn@MgO-P3000.[29] In another model system, the CuAgNiFeCoRuMn@MgO-P3000 catalyst exhibited unique catalytic performance and high stability, which are challenging to achieve in heterogeneous catalysis research and enable allowing reduction of nitroarenes within 60 s leading to high conversion approaching 100% for the production of the corresponding amino compounds under mild conditions. This catalyst exhibited high catalytic stability and recyclability along with strongly inhibited sintering and aggregation due to the strong us-MEA-NP–support interactions. The atoms in the MEA-NPs have different densities of states (DOSs); in other words, some atoms lose their elemental identity, and the DOS can be tuned by adjusting the neighboring atoms. The probable electronic structure changes were studied based on supervised learning.[29] This approach paves the way toward achieving stable catalysts and constructing effective NPs for a variety of applications.

2 | RESULTS

2.1 | Rational design of MEA NPs with up to septenary mixing

Conventionally, fast-moving bed pyrolysis, the solvothermal method, top-down lithography, vapor-phase deposition and CTS (Joule heating) can generate many us-MEA-NPs via pyrolysis of mixed precursors loaded on various electrically conductive supports (i.e., carbon, zeolite, γ-Al_2O_3, and black and graphene oxide); however, these methods require several steps and costly equipment and are suitable for limited combinations of strongly repulsive metallic elements and supports.[30,31] In contrast, a series of us-MEA-NPs, from ternary (CuAgCo) to quinary (CuAgCoNiFe) and septenary (CuAgNiFeCoRuMn) us-MEA-NPs, were synthesized via a straightforward one-pot water-based solution method. An equimolar mixture of salt precursors $M_x(NO_3)_y$ (M is Ag, Co, Cu, Ni, Fe, Ru, or Mn) was used in the a facile one-pot U-SEO-P synthesis method at 0°C with a short treatment time (60 s) (further information in Supporting Information with Figures S1 and S2). The ultrasonic frequency (28, 40, and 138 kHz) (Figure S3) and high-electric field plasma discharge induced rapid dissolution of the hydrolyzed precursors to form mixed metal atoms. This process caused growth and rupture of microbubbles in regions with local

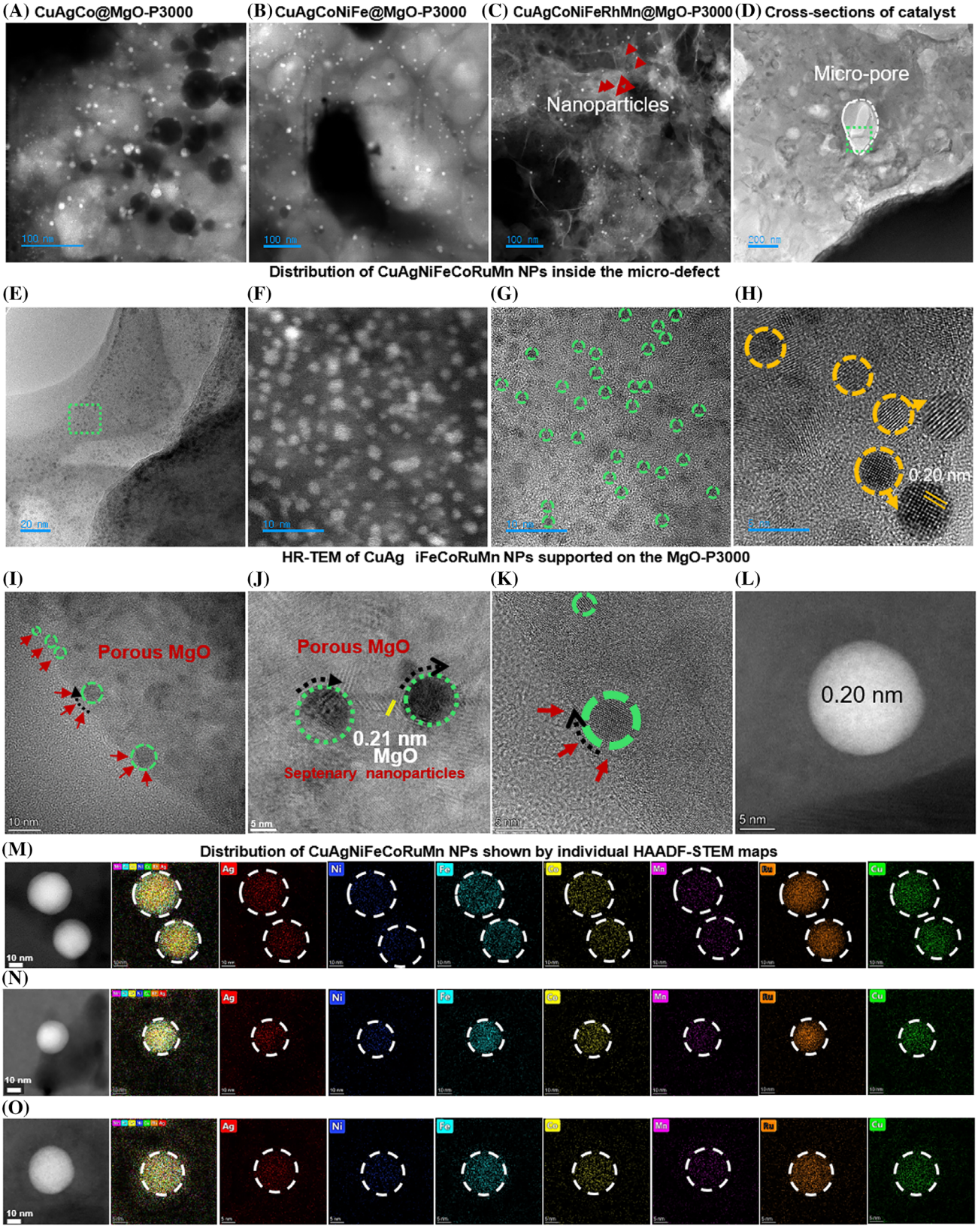

FIGURE 1 HR-TEM images of (A) ternary (CuAgCo), (B) quinary (CuAgCoNiFe), and (C) septenary (CuAgNiFeCoRuMn) us-MEA-NPs encapsulated within MgO-P3000. (D–H) HR-TEM images of CuAgNiFeCoRuMn NPs on cross-sections of MgO-P3000. (I–L) Distribution of CuAgNiFeCoRuMn inside micropores and on the surface of the MgO-P3000 support. (M–O) High-angle annular dark-field (HAADF) scanning TEM (STEM) images and EDS chemical maps of Cu, Ag, Ni, Fe, Co, Ru, and Mn in CuAgNiFeCoRuMn@MgO-P3000 in different areas from (F).

plasma temperatures higher than 3000 K, which rapidly increased over a short time in the discharge channels. Rapid oxidation of the magnesium metal plate occurred when molten Mg left the channels; this oxidation promoted the combination of the porous MgO-P3000 support and metal ions through the uniform formation of well-mixed us-MEA-NP droplets during reduction, which rapidly cooled at the surface support interface (Scheme 1). We consider the higher temperature (~3000 K) here to be the reason for the distribution of NPs on the porous MgO-P3000 film, which absorbed ultrasonic radiation and converted it into thermal energy more efficiently than MgO powder or porous wood. The temperature was significantly greater than the melting points of the metals and decomposition temperatures of the metal precursor salts (Table S1), facilitating reduction of the metal ions and formation of solid solution particles while avoiding oxide impurities. In addition to this high temperature effect, the ultrasonic energy enhanced the chemical reactions and chemical agent-free reduction of precursors via thermal dissociation (pyrolysis combined with the physical effects of ultrasound) of H_2O molecules, generating extremely reactive free radicals, including $H^{\bullet}$ and $OH^{\bullet}$ (Equation 1).

$$H_2O + \text{ultrasound} \rightarrow e^-_{aq,}\ H_3O^+, H^{\bullet}, H_2, OH^{\bullet}, H_2O_2. \quad (1)$$

The ternary (CuAgCo), quinary (CuAgCoNiFe), and septenary (CuAgNiFeCoRuMn) us-MEA-NPs, which were similar in size (diameter of 2–5 nm) regardless of the multielement combination or composition, were uniformly distributed on the surface of the porous MgO-P3000 support without significant aggregation and were incompletely encapsulated by the support material, leaving a partially exposed free surface (Figure 1A–C). Despite the variations in the porosity of MgO-P3000 after reduction at high temperatures, the growth of us-MEA-NPs inside the pores resulted in comparable particle size distributions (Figure 1E–H). The as-prepared CuAgNiFeCoRuMn us-MEA-NPs were uniformly distributed and crystallized on the MgO-P3000 support (Figure 1H). Moreover, x-ray diffraction confirmed the close interfacial interactions between the MEA-NPs and MgO-P3000 (Figure S4). Accordingly, the seven metal elements in the CuAgNiFeCoRuMn us-MEA-NPs formed a face-centered cubic (FCC) structure with a lattice constant of 0.21 nm, as shown by the electron diffraction ring pattern. Moreover, the lattice spacing of 0.21 nm between adjacent lattice fringes of the CuAgNiFeCoRuMn us-MEA-NPs was indexed to the *d* spacing of the (111) plane of the FCC structure. The CuAgNiFeCoRuMn us-MEA-NPs in CuAgNiFeCoRuMn@MgO-P3000 were generally smaller than 4 nm and had an average size of 2 nm (Figure 1C) inside and outside the micropores. The high-resolution transmission electron microscopy (HR-TEM) images showed an overlayer covering the us-MEA-NPs of the CuAgCo@MgO-P3000, CuAgCoNiFe@MgO-P3000, and CuAgNiFeCoRuMn@MgO-P3000 samples (Figure 1I–K; any structural changes that may have been induced by the electron beam were excluded); the layer boundaries within the regions containing us-MEA-NPs were constant, consistent with the expected features of an encapsulated structure.[32] To confirm the well-mixed homogeneous nature of the us-MEA-NPs, we performed energy-dispersive x-ray spectroscopy (EDS) TEM mapping. Elemental analysis (Figure 1L–O) of CuAgNiFeCoRuMn@MgO-P3000 confirmed that the seven elements were uniformly distributed in representative Cu-Ag-Ni-Fe-Co-Ru-Mn-NPs, with no evidence of phase separation or single metal segregation in the NPs; that is, CuAgNiFeCoRuMn-NP solid-solution alloys were generated. In order to further prove that the proportion of each element is equal to the desired ratio of metals, we used inductively coupled plasma optical emission spectroscopy (ICP-OES) to analyze the composition of us-MEA-NPs (Table S2).

After facile one-pot U-SEO-P synthesis, the us-MEA-NPs were uniformly distributed on the MgO-P3000 film, with an average size of ~2.1 nm (Figure 2A; 100 particles were measured). These NPs exhibited a homogeneous distribution and a very narrow size distribution, with approximately 98% of the us-MEA-NPs having a size smaller than 2.5 nm. CuAgNiFeCoRuMn@MgO-P3000 was also prepared by the conventional deposition-precipitation method under the same conditions. The us-MEA-NPs@MgO-P3000 catalyst, which was composed of CuAgNiFeCoRuMn-NPs supported on MgO-P3000, was prepared by anchoring us-MEA-NPs synthesized via CTS heating onto MgO powder.[33] The CuAgNiFeCoRuMn NPs prepared by the conventional method (e.g., deposition-precipitation [DP] method) quickly formed particles measuring ~5.02 nm after calcination at 400°C (Figure 2B) (for more details, see Reference [32]). As expected, the us-MEA-NPs@MgO catalyst prepared by the DP method had no special embedded configuration for anchoring us-MEA-NPs on the support surface, which led to weak catalyst support interactions[34] and poor sintering resistance at high temperatures and in water.

Moreover, x-ray photoelectron spectroscopy (XPS) of the surface (~1 nm in depth, as determined by the Al Kα beam energy) revealed that all the elements were present in the us-MEA-NPs and indicated the presence of interatomic interactions as well as surface oxidation of the NPs (Figure 2). The core Ag $3d_{3/2}$, Cu $2p_{3/2}$, Ni $2p_{3/2}$, Fe $2p_{3/2}$, Co $2p_{3/2}$, Ru $2p_{3/2}$, Mn $2p_{3/2}$, and Mg 1s binding energies were measured for each sample, and the peaks were deconvoluted. The peaks corresponding to

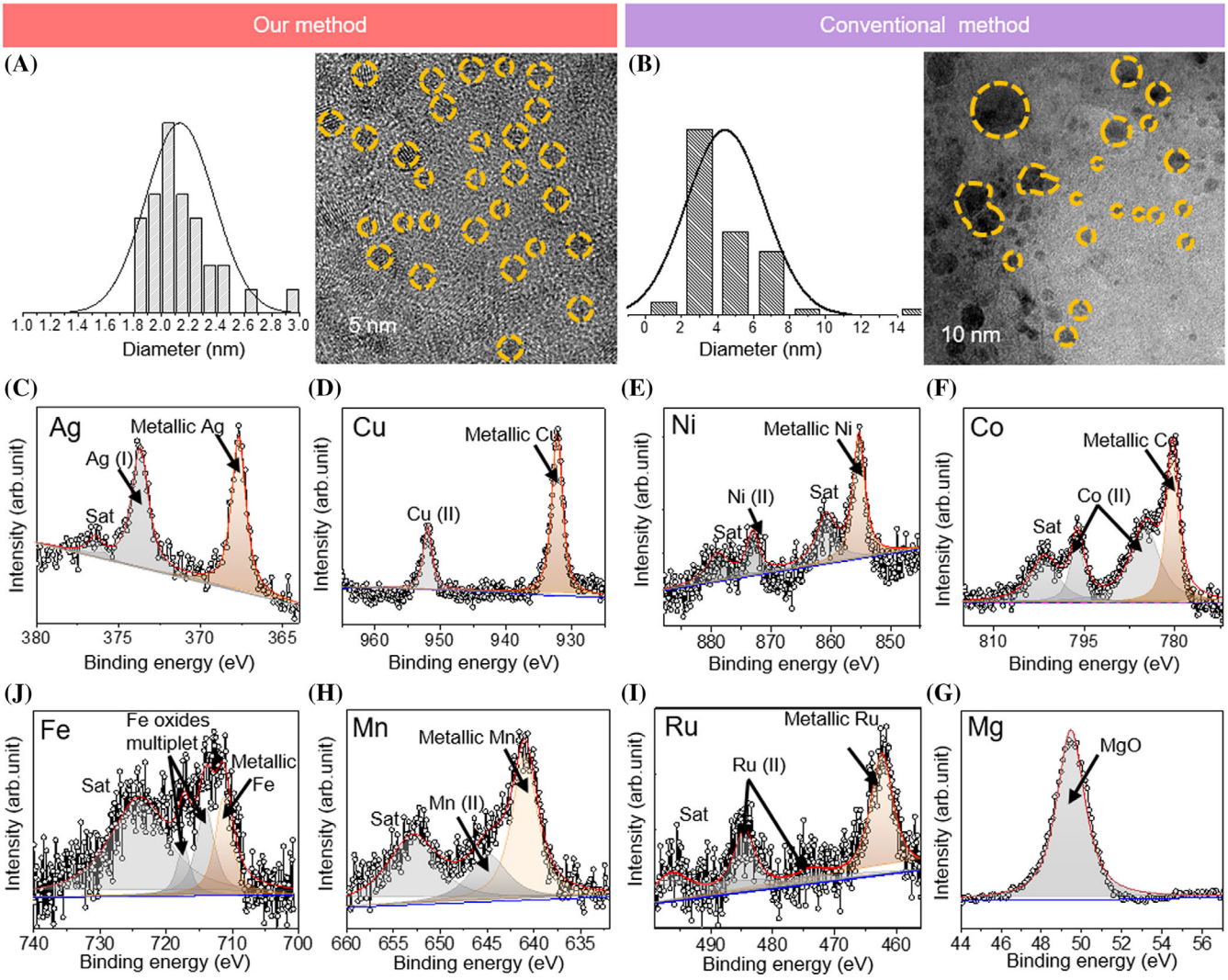

FIGURE 2 Characterization of CuAgNiFeCoRuMn NPs supported on MgO-P3000 synthesized via the DP method and our method. (A and B) TEM images and histograms showing the particle size distributions of CuAgNiFeCoRuMn NPs on MgO-P3000 for each method. XPS data showing the (C) Ag 3d, (D) Cu 2p, (E) Ni 2p, (F) Co 2p, (J) Fe 2p, (H) Mn 2p, (I) Ru 2p, and (G) Mg 1s binding energies.

the elemental metals are presented with orange shaded lines in Figures 2C–G and were separately extracted for each of the CuAgNiFeCoRuMn/MgO-P3000 catalysts. The core-level shifts (CLSs) relative to the pure metals were consistent with previous reports on bimetallic systems[35] and indicated that the underlying electronic structures of the MEA systems were dissimilar to those of pure metals. The CLSs for any given elemental component were in the same direction for each of the catalysts consisting of us-MEA-NPs on MgO. Moreover, the CLSs of the Mn 2p, Mg 1s, Fe 2p, Co 2p, and Ni 2p spectra were all in the direction of higher binding energies, whereas that of Cu 2p was in the direction of lower binding energies (Figure 2D and Figure S5). These effects can be attributed to interatomic electron transfer between the materials and relaxation effects arising from core-hole screening around the atoms.[36] Thus, during MEA-NP formation in CuAgNiFeCoRuMn@MgO-P3000, some of the metal atoms likely acted as electron acceptors (negative shift) or electron donors (positive shift) for other metals (Figures S5 and S6). To further examine this hypothesis, we prepared us-MEA-NPs with the more electronegative element Ru (CuAgNiFeCoRuMn@MgO-P3000) to examine the behavior of the Cu core. The Cu binding energy in CuAgNiFeCoRuMn@MgO-P3000 shifted to a lower value, indicating that Cu changed from a net electron acceptor to an electron donor.

NP models were built from the relaxed CuAgNiFeCoRuMn unit cell after geometry optimization (see Section 5 for details), as shown in Figure 3A–C. The projected total DOS (PDOS) is displayed in Figure 3D. The energy sequence, based on the center of each PDOS (at 50% occupancy), was Ag-3d, Cu-3d, Ru-4d/Rh-4d, Ni-3d, Co-3d, Fe-3d, and Mn-3d. Accordingly, the states

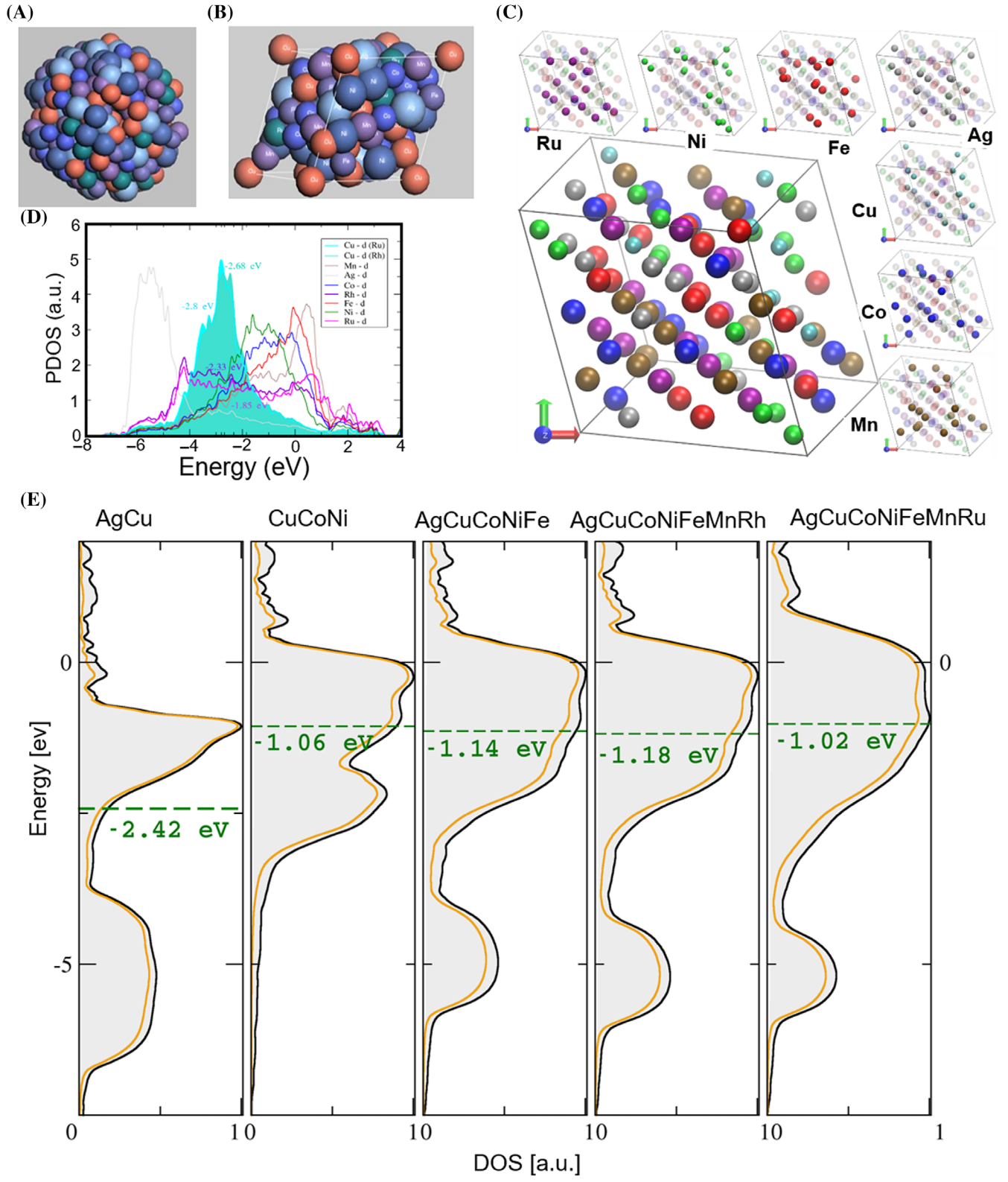

FIGURE 3 (A) Model of a CuAgNiFeCoRuMn NP obtained from (B) the relaxed unit cell. (C) Detailed atomic arrangements within the relaxed unit cell-smaller boxes show the distribution of each atomic species. (D) PDOSs of CuAgNiFeCoRuMn and CuAgNiFeCoRhMn—the Cu-3d states for the Ru- and Rh-containing NPs are shown, and their energies are indicated. A shift in the Cu 3d states to higher energies upon Ru replacement by Rh is observed. (E) DOS and PDOS for the sequence AgCu NPs, CuCoNi NPs, AgCuCoNiFe NPs, AgCuCoNiFeMnRh NPs and AgCuCoNiFeMnRu NPs. Atom colors: Fe (red), Mn (brown), Ni (bright green), Co (blue), Ru (purple), Cu (cyan), Ag (silver), H (white), and N (grass green).

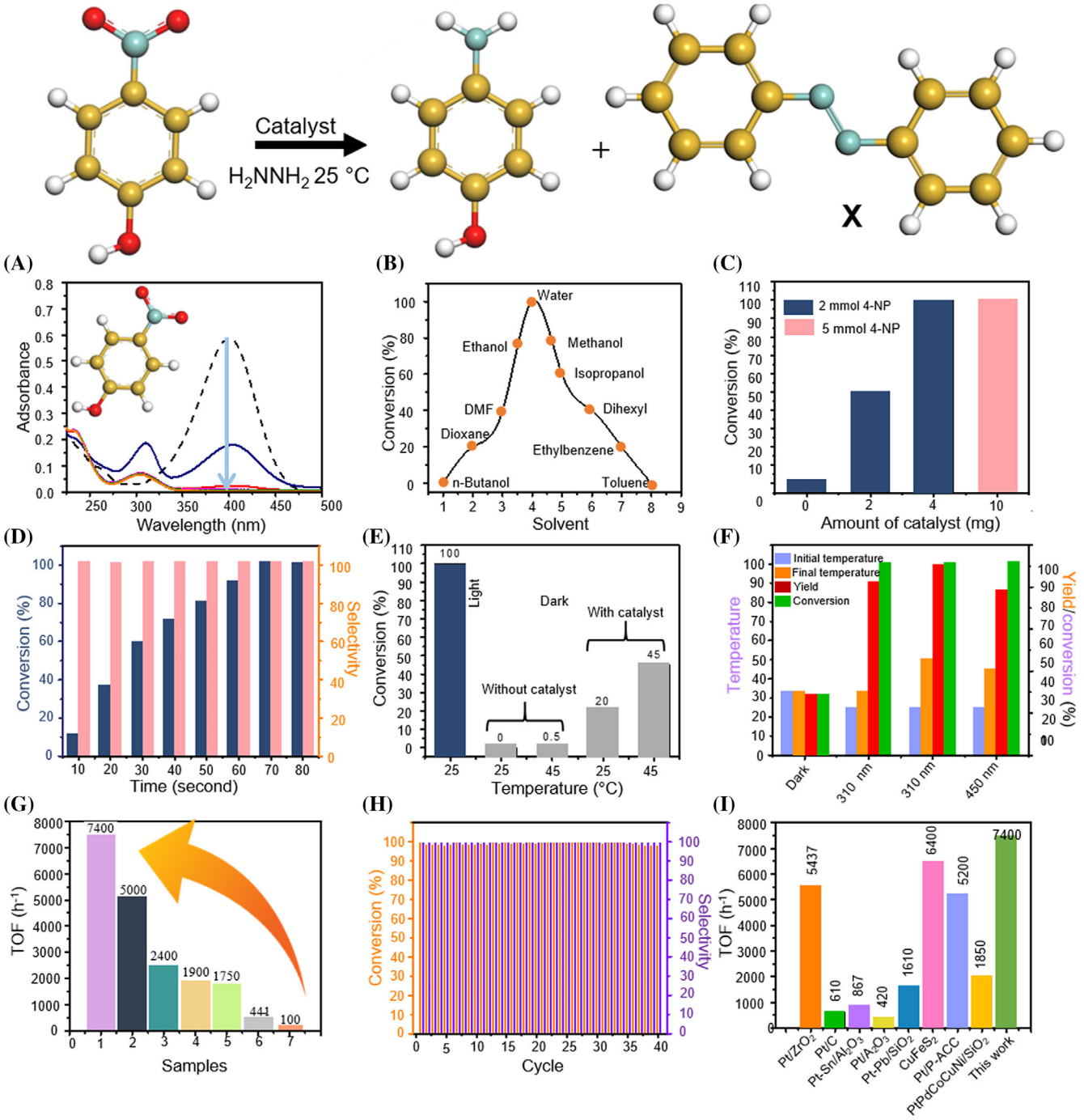

FIGURE 4 Catalytic activity of CuAgNiFeCoRuMn@MgO-P3000 in the hydrogenation of 4-NP. (A) UV–vis spectra of 4-NP on selected samples. (B) Solvent selection. (C) Catalyst amount. (D) Conversion and selectivity. (E) 4-NP conversion at different temperatures. (F) Reduction reaction with temperature control in the dark or under light irradiation. (G) TOF values of different samples (1: CuAgNiFeCoRuMn@MgO-P3000, 2: CuAgNiFeCo@MgO-P3000, 3: CuAgFeCo@MgO-P3000, 4: CuAgCo@MgO-P3000, 5: CuAg@MgO-P3000, 6: Ag@MgO-P3000). (H) Results of recycling CuAgNiFeCoRuMn@MgO-P3000 in the 4-NP reaction. (I) Comparison of the TOF values of different catalyst systems.

at the Fermi level mainly included Mn and Fe states, followed by Ru and Co states. We therefore expect the reactivity to be driven by Mn and Fe. Upon replacement of Ru with Rh, the Cu 3d energy shifted from −2.8 eV (Ru) to −2.68 eV (Rh) (the corresponding Cu 3d peaks for Ru and Rh are shown in Figure 3D in cyan and turquoise, respectively, together with their energies). The energy of Rh states was lower (−2.33 eV) than that of the Ru states (−1.85 eV). The energy of the Fe states also shifted to a slightly higher value (−0.73 to −0.66 eV)

upon replacement of Ru with Rh. DOS and PDOS were calculated for the sequence AgCu, CuCoNi, AgCuCoNiFe, AgCuCoNiFeMnRh, and AgCuCoNiFeMnRu (Figure 3E), using a CPA impurity model to simulate the disordered supercells (see Supporting Information for details). The inclusion of both Cu and Ag, and the replacement of Rh by Ru, lead to a fine-tuning of the electronic properties of the AgCuCoNiFeMnRu NPs, which show the largest relative amount of empty states above the Fermi level (mainly Fe/Mn/Co, then Ni, all relevant as active site), accompanied by a lowering of low-energy states and higher chemical potential of *d* states, consistent with the analysis performed on a specific NP model (see Figure 3). Besides further activating Fe/Mn/Co/Ni states, Ru is playing a global role of electronic property and reactivity optimization, well beyond its contribution to enhancing configurational entropy.

2.2 | Reduction with the CuAgNiFeCoRuMn@MgO-P3000 catalyst

The catalytic hydrogenation of 4-nitrophenol (4-NP), a model substrate, to 4-aminophenol (4-AP) by CuAgNiFeCoRuMn@MgO-P3000 was examined under mild conditions with hydrazine and 2-propanol (secondary alcohol) as the hydrogen sources at 25°C. Figure 4A shows the conversion of 4-NP obtained for each catalyst after 60 s of reduction. CuAgNiFeCoRuMn@MgO-P3000 showed high conversion (100% at 1 min), whereas the other catalysts (i.e., CuAgCo@MgO-P3000 and CuAgCoNiFe@MgO-P3000) delivered slightly lower conversions of 90% and 95%, respectively, at 1 min. We screened several solvents and found that water was the optimum solvent for our catalytic system. CuAgNiFeCoRuMn@MgO-P3000 exhibited exceptional catalytic activity in water and protic solvents (such as methanol and ethanol). In contrast, the catalytic activity was lower in solvents such as tetrahydrofuran, n-butanol, toluene, isopropanol, dioxane, and *N*,*N*-dimethylformamide (DMF) (Figure 4B). These results are consistent with previous reports that protic solvents can transport hydrides from active sites to substrates and thus enhance the hydrogenation reaction (Figure 4B).[37] The conversion of 4-NP and the reaction rate depended on the catalyst amount; a maximum yield of 100% and a turnover frequency (TOF) of 7400 h^{-1} were obtained with an optimal ratio of 10 mg catalyst/5 mmol 4-NP (Figure 4C). In the absence of a catalyst or a reducing agent, the reaction did not produce any 4-AP under natural light or darkness, demonstrating the excellent catalytic performance of CuAgNiFeCoRuMn@MgO-P3000. The above TOF was substantially greater than those previously reported for thermal catalysts or photocatalysts for the reduction of nitro compounds (Table S1). In addition, CuAgNiFeCoRuMn@MgO-P3000 exhibited an exceptionally strong catalytic performance (100% conversion and 100% selectivity within 60 s) (Figure 4D).

To gain further insight, control reactions were performed in the dark in a water bath at 25 or 45°C, which afforded 4-AP with conversions of 20% and 45%, respectively (Figure 4E), confirming that CuAgNiFeCoRuMn@MgO-P3000 is intrinsically active, which is a significant feature of an ideal photocatalyst.[38] The control reduction reactions in the dark in a water bath at 25 or 45°C delivered lower conversions than the reaction at 25°C under light, indicating that the CuAgNiFeCoRuMn@MgO-P3000 acts via intermediate photoexcited species and photothermal activation. As a result, CuAgNiFeCoRuMn@MgO-P3000 may be considered a photothermal agent; thus, irradiation (UV light source, $\lambda \approx 310$ nm) during the catalytic reaction produced a natural temperature increase to 50°C (Figure 4F, "light without the cooling system").[39] When the same catalytic reaction was carried out while using the cooling system of the photoreactor, the temperature was 25°C, and a somewhat lower yield of 90% was obtained, with 100% 4-AP conversion (Figure 4F, "light with the cooling system"). CuAgNiFeCoRuMn@MgO-P3000 exhibited extremely high catalytic activity, with a TOF of 7400 h^{-1} (Figure 4G), suggesting the indispensable roles and unique properties of Ru, Fe, and Mn species as electron-enriched active sites in nitrophenol hydrogenation reactions, as confirmed by DOS results (Figure 3D,E). From out MD simulations and electronic structure calculations, we can support the scenario of active sites on the surface of the NP, to which Mn, Fe, and Ru belong. However, Ag and Cu are equally important to help fine-tuning the overall electronic properties of NP, in particular in shifting atomic states to different energies, like demonstrated in our previous and new DOS/PDOS analysis. For the magnesium oxide-supported metal atoms in CuAgNiFeCoRuMn, H_2 activation (1/2 $H_2 \rightarrow H^*$) preferentially occurred at the metal sites, and the activation energies for H_2 (1/2 $H_2 \rightarrow H^*$) on Cu, Ag, Ni, Fe, Co, Ru, and Mn differed according to the DFT results.

CuAgCoNiFe@MgO-P3000 showed a low TOF of 2400 h^{-1}, which might have resulted from the absence of active sites such as Ru and Mn. The use of CuAgCo@MgO-P3000 and AgCo@MgO-P3000 yielded 4-AP with low TOF values of 1900 and 1750 h^{-1}, respectively, along with slow 4-NP conversion. These results were consistent with our report[39] that Ni, Fe, Ru, and Mn provided binding sites for NH_2NH_2 via strong physical adsorption, while in their absence, the number of hydrogen adsorption sites decreased. Notably, the CuAgNiFeCoRuMn@MgO-P3000 system exhibited

excellent stability for 40 cycles in terms of both conversion and selectivity without loss of catalytic activity (Figure 4H). Additionally, inductively coupled plasma atomic emission spectroscopy (ICP-AES) characterization of the spent catalyst revealed no noticeable structural changes and no metal leaching (i.e., only 0.020 at. % of CuAgNiFeCoRuMn atoms fell off the fresh catalyst) in aqueous solution. CuAgNiFeCoRuMn NPs still keep the same dispersions with unchanged morphological features and chemical composition after cycling tests, as shown in Figures S7–S9, demonstrating that the CuAgNiFeCoRuMn@MgO-P3000 remains active with remarkable catalytic stability. This is attributed to the strong electronic multielements metal-support interactions between unsymmetrical CuAgNiFeCoRuMn NPs configuration and the MgO-P3000 support. The HRTEM and STEM results shown the strong metal-support interactions between the us-MEA-NPs and the MgO-P3000 support, as shown in Figure S8. These consequences clarified the structural advantages of CuAgNiFeCoRuMn@MgO-P3000, which had an embedded structure and strong us-MEA-MgO-P3000 interactions that stabilized the CuAgNiFeCoRuMn NPs against leaching, inducing the improved capability for H_2 dissociation, the easy release of the products to prohibit over hydrogenation and dehalogenation and the re-exposure of the surface active site for the coming hydrogenation. Furthermore, the recycled and fresh catalysts exhibited similar morphologies and composition (Figures S8 and S9 and Table S3).

2.3 | Benchmarking of the us-MEA-NP catalyst

The CuAgNiFeCoRuMn@MgO-P3000 catalyst prepared via the U-SEO-P approach was stable for 40 cycles and maintaining its catalytic activity (4-NP yield of ∼100%), while the other catalysts prepared via different methods exhibited stability for fewer than 40 cycles during reduction in an aqueous solution. Based on the above analysis, CuAgNiFeCoRuMn@MgO-P3000 exhibited remarkable reduction activity compared to that reported in the literature (Figure 4I and Table S1), as confirmed by its conversion activity and TOFs.[40] These results are due to the unexpected synergistic responses, along with the high surface-to-volume ratios, arising from the mutual electronic interactions between the constituent elements, resulting in multielement active sites on CuAgNiFeCoRuMn@MgO-P3000. In addition, the chemical and electronic behavior of us-MEA-NPs is different from that of their compositionally simpler counterparts and facilitates improved catalytic functions. Furthermore, CuAgNiFeCoRuMn@MgO-P3000 could be easily separated from the aqueous phase. In contrast, most catalysts require sophisticated approaches for extraction from the reaction solution.

2.4 | Simulations of the adsorption

To understand the reactivity of the CuAgNiFeCoRuMn NP surfaces and the role of atomic sites, simulations of the adsorption and decomposition of H_2 and N_2H_4 on ∼2 nm NPs were performed. The NP model was built based on the geometry optimized periodic model (see Section 5 and Supporting Information for details). Hydrazine (Figure 5A) was preferentially adsorbed at Mn (brown)/Fe (red) sites (0.0–0.15 ps) and then underwent splitting processes that also involved Ni sites (0.15–0.43 ps, transparent green). For H_2, the simulations showed preferential adsorption at Fe/Ru sites, followed by rapid dissociation and desorption of the active species (Figure 5B). MD calculations show that 4-NP has a strong affinity for Fe/Mn/Ni-rich sites (red/brown/green atoms), with Ru in proximity (purple atom). Bonding to the surface of the NP entails a strong rehybridization around N (Figure 5C, 20 ps), under partial rearrangement of the NP surface, which takes a Fe atom closer to N and Mn/Ni closer to O (20–40 ps). Within our simulations, fluctuations of the surface lead to the elongation of a N—O bond (40 ps).

2.5 | Substrate scope for the CuAgNiFeCoRuMn@MgO-P3000 catalyst

Given the high catalytic activity of CuAgNiFeCoRuMn@MgO-P3000, we investigated its use for a wide variety of substrates irrespective of the presence of different functionalities (Scheme 2). Excitingly, substrates with electron-acceptor and electron-donor groups, especially at the para position, were reduced under visible light to the corresponding amines with excellent conversion and selectivity at room temperature. Overall, substrates with electron acceptors, such as —NO_2, —CHO, and —Cl, exhibited much greater conversions of aldehydes and nitro compounds. In contrast, the presence of electron donors, such as —NH_2 and —CH_3, decreased the conversion of nitro compounds. This difference is due to the decrease in the charge on the NO_2 group in the presence of an electron acceptor in the aromatic ring, which activates nitro compounds toward reduction. Additionally, in the presence of an electron donor in the aromatic ring,

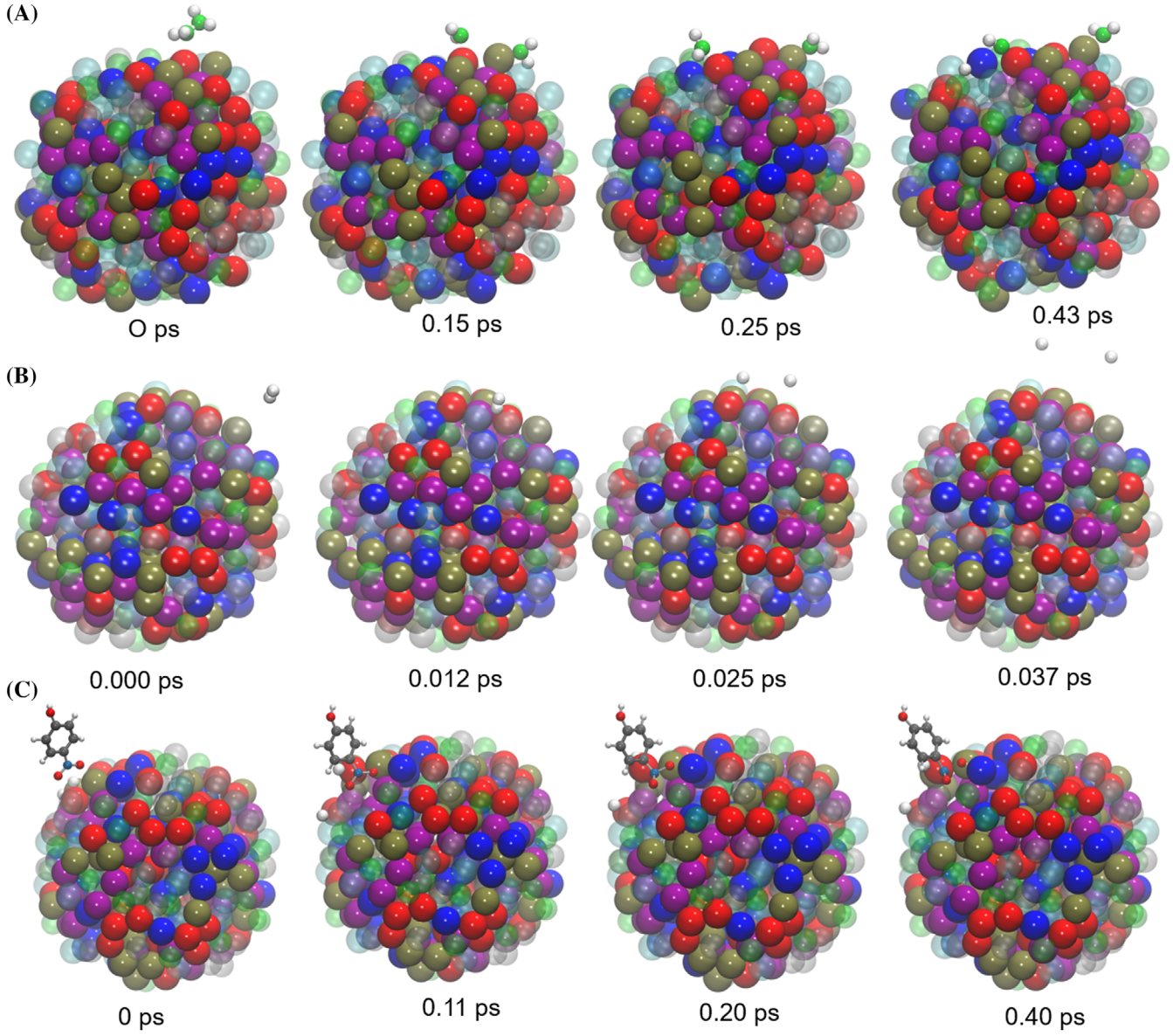

FIGURE 5 Adsorption and activation of N_2H_4/4-NP and H_2 on CuAgNiFeCoRuMn NPs; (A) N_2H_4 adsorption at Mn/Fe sites, followed by N-N bond breaking (0.15 ps), surface diffusion and further fragmentation at Fe/Ni sites (0.25–0.43 ps). (B) H_2 adsorption (0.012 ps), dissociation and desorption (0.037 ps). (C) 4-NP adsorption (0.011 ps), dissociation and desorption (0.40 ps). Atom colors: Fe (red), Mn (brown), Ni (bright green), Co (blue), Ru (purple), Cu (cyan), Ag (silver), H (white), and N (grass green).

the ability of NO_2 to receive electrons is weakened, and NO_2 cannot be reduced. Para-substituted compounds showed higher conversions than meta-substituted in the reduction of nitroarenes to the corresponding amino compounds with either electron acceptors or electron donors, such as NH_2 and NO_2. Substrates containing carbonyl groups were reduced to hydroxyl groups. In addition, when the compounds contained heterocyclic aromatic rings, CuAgNiFeCoRuMn@MgO-P3000 catalyzed the hydrogenation of nitro groups to amino groups without destroying the heterocyclic compounds.

3 | DISCUSSION

In the synthesis of CuAgNiFeCoRuMn@MgO-P3000, we used a high local plasma temperature and a high-entropy process ($T\Delta S_{mix}$) to form small liquid droplets of us-MEA-NPs to thermodynamically drive the formation of alloys with specific compositions. The U-SEO-P process enabled the formation of homogeneous us-MEA-NPs by inducing a high local temperature that increased the entropy contribution ($T\Delta S_{mix}$) (expressed as $\Delta S_{mix} = -R\sum_{i=1}^{n} c_i lnc_i$, where c_i is the molar fraction of

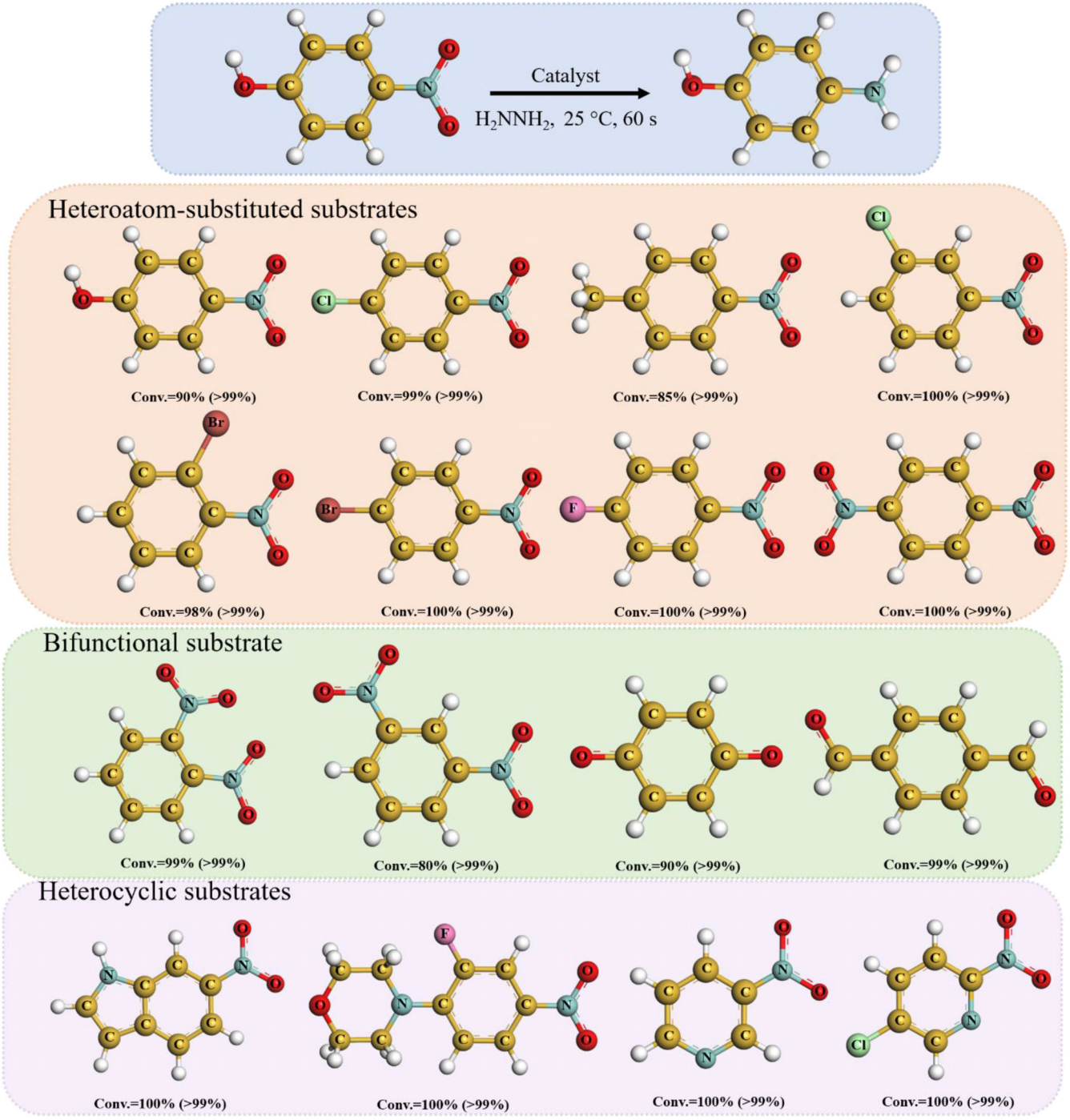

SCHEME 2 Scope for the hydrogenation of various organic compounds in water with CuAgNiFeCoRuMn NPs.

the *i*th element, R is the molar gas constant, and n is the total number of metallic elements).[40–42] As an example, Figure 6 A and B show the contour maps of ΔH_{mix} and ΔS_{mix} for the CuAgCo system as a model ternary alloy. The energy gain in the most of the metallic alloys was sufficient for ΔS_{mix} stabilization of the random solid-solution phase against the intermetallic catalysts according to Richard's rule.[10] Therefore, the mixing entropy ΔS_{mix} for equiatomic us-MEA-NPs is given by Equation (2).[43–47]

$$\Delta S_{mix} = R \ln n. \quad (2)$$

Consistent with the "high-entropy" effect, the random solid solution was stabilized in the presence of several metallic elements mixed together in equimolar proportions. A larger ΔS_{mix} (ΔS_{mix} scaled vs. $ln\ n$) was achieved for metallic alloys with a greater number of metal elements, thus increasing the probability of solid solution formation according to Equation (2). In general, the

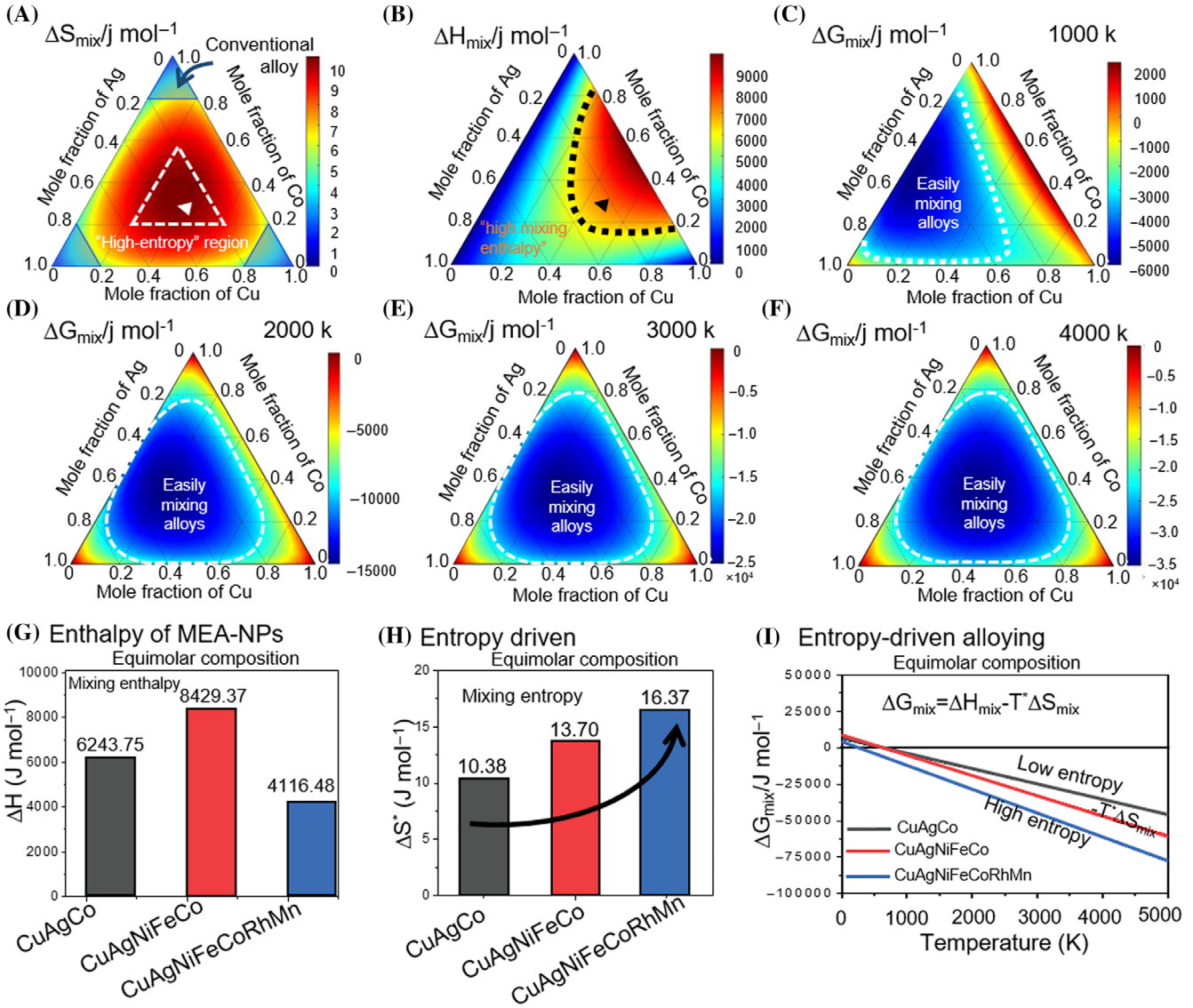

FIGURE 6 Computational study of alloy formation by the us-MEA-NPs. (A) Contour plot of the mixing entropy (ΔS_{mix}) (J/mol K) of the CuAgCo system. The red central region represents the "high-entropy region", whereas the blue corner regions represent the conventional regions. (B) Contour plot of the mixing enthalpy (ΔH_{mix}) (J/mol K) of the CuAgCo system. The red region indicates the "high-enthalpy region", whereas the blue peripheral regions indicate high miscibility. (C–F) Temperature-dependent Gibbs free energy (ΔG_{mix}) of the CuAgCo-NPs derived from thermodynamic calculations. The blue central region indicates the "easily mixed alloys". (G) Mixing enthalpy (ΔH_{mix}), (H) mixing entropy (ΔS_{mix}), and (I) temperature-dependent Gibbs free energy (ΔG_{mix}) of CuAgCo-NPs, CuAgNiFeCo-NPs, and CuAgNiFeCoRuMn-NPs derived from thermodynamic calculations. us-MEA-NPs with a higher ΔS_{mix} formed an alloy phase at a low temperature owing to the entropy effect ($-T\Delta S_{mix}$).

formation of a single-phase solid solution has an enthalpy window of -15 kJ mol^{-1} < ΔH_{mix} <5 kJ mL^{-1}, which is consistent with the results of Zhang *et al.*[5] In our work, the synthesis of CuAgNiFeCoRuMn@MgO-P300 involved synergy between high entropy and high temperature, which was achieved by ultrasonic irradiation. Thermodynamically, the mixing Gibbs free energy (ΔG_{mix}) is the sum of two terms, that is, the mixing enthalpy (ΔH_{mix}) and the mixing entropy (ΔS_{mix}) (Equation 3):

$$\Delta G_{mix} = \Delta H_{mix} - T\Delta S_{mix}. \quad (3)$$

ΔH_{mix} is related to the atomic bonding energy according to a quasichemical model and does not depend on the number of components (n) in the system. For example, ΔH_{mix} did not show a monotonic trend as n increased from 3 to 7 in the CuAgCo system (Figure 6A). In contrast, ΔS_{mix} increases when more components are introduced into a system (Figure 6B) because a higher n results in a higher configurational

entropy. If ΔG_{mix} is plotted against temperature (Figure 6C), then ΔS_{mix} is given by the slope of the curve. Thus, decreasing ΔG_{mix}, that is, stabilizing a single phase by increasing the temperature, was most effective at $n = 7$. In addition, the high temperature resulting from plasma discharge and ultrasonic irradiation was essential for realizing high entropy ($\Delta G_{mix} = \Delta H_{mix} - T\Delta S_{mix}$). In the CuAgCo system, for example, although ΔH_{mix} peaked when the mole fraction of Ag was zero, the peak for ΔS_{mix} occurred at a near-equimolar composition (Figure 6D,E). Thus, ΔH_{mix} strongly affects ΔG_{mix} at low temperatures (1000 K), but its effect becomes negligible as the temperature increases to above 2000 K (Figure 6F–I). Consequently, ΔG_{mix} can be controlled almost solely by ΔS_{mix} at the high temperatures caused by plasma discharge and ultrasonic irradiation, which induces severe lattice distortion and slow in-depth diffusion, stabilizing the structures of metallic alloys against nanoscale phase separation and elemental aggregation and confirming the presence of a solid-solution structure.

Mixing is spontaneous at $\Delta G_{mix} < 0$, and $|\Delta G_{mix}|$ is the driving force for mixing. For the systems with 3, 5, and 7 components, ΔG_{mix} was 0 at 601, 615, and 251, respectively, and ΔG_{mix} became increasingly negative with a greater number of components due to the greater ΔS_{mix} (Figure 6C). Notably, NP formation induced lattice strain due to the incorporation of multiple elements with higher n values. However, the steeper ΔG_{mix} gradient in a higher n system can compensate for the lattice strain at the very high temperatures (~3000 K) generated by plasma discharge and ultrasonic irradiation. In conclusion, the higher ΔG_{mix} and atomic diffusion at high temperature played important roles in NP formation. In addition to influencing the temperature, the ultrasonic energy and plasma discharge broadly excited the vibrational degrees of freedom; thus, the unfavorable ΔH_{mix} was exceeded by the ΔS_{mix} contribution (Figure 6), and the us-MEA-NP system was entirely miscible. Numerous nucleation sites appeared due to vibrations, which provided a uniform distribution and refinement of the NPs. Therefore, the synergistic effect of the electric field with ultrasonic irradiation successfully generated alloy mixtures, but precise evaluation of each contributing parameter requires additional trials and possibly a data-driven discovery approach. The MEA-NPs aided in metallic alloy formation by increasing the entropy ($\Delta G_{mix}\downarrow = \Delta H_{mix} - T\Delta S_{mix}$), and the higher entropy resulted in severe lattice distortion and slow in-depth diffusion, thus stabilizing the structures of the metallic alloys against nanoscale phase separation and elemental aggregation and confirming the presence of a solid-solution structure.

4 | CONCLUSIONS

In summary, we developed a scalable synthetic approach (simultaneous electrooxidation-reduction-precipitation strategy) to prepare a series of us-MEA-NP systems with strongly immiscible element pairs. This strategy provides (i) an excellent platform for synthesizing us-MEA-NPs@MgO-P3000 with (ii) tunability, (iii) generality, and (iv) potential scalability. The local plasma electron temperature in plasma channels under ultrasonic irradiation in this approach (reaching 3000 K) was higher than the decomposition temperatures of all of the metal precursors, which enabled uniform mixing of nearly any metallic combination (i.e., generality). Accurate control of the ultrasonic-assisted combined electrooxidation–reduction parameters (i.e., ultrasonic irradiation, temperature, substrate, plasma discharge duration, and heating/cooling rate) affected the dispersity, final structure, and size of the particle. The easily tunable synthesis of a unique embedded support (i.e., MgO-P3000) for stabilization and dispersion of us-MEA-NPs on its surface with a high entropy contribution, a high local temperature and ultrasonic energy is ideal for large-scale nanomanufacturing, where energy-efficient (instant heating through an electric field) and rapid (within milliseconds) synthetic processes could enable the high-volume production of high-quality us-MEA-NPs@MgO-P3000. These U-SEO-P-prepared materials represent a new area of research for material discovery and optimization in which the mixing entropy of us-MEA-NPs and the elemental composition of the support surface can be designed and controlled. More importantly, CuAgNiFeCoRuMn@MgO-P3000 exhibited significant catalytic activity, excellent recyclability, durability, and stability during the reduction of nitro groups to amino groups.

5 | EXPERIMENTAL SECTION

All the experimental procedures are described in the Supporting Information.

5.1 | Manufacture of the alloy us-MEA-NPs@ MgO-P3000

Plate-type samples of an AZ31 Mg alloy (Al 3.08 wt%, Zn 0.76%, Mn 0.15%, Mg balance) were coated via U-SEO-P by applying a 60 Hz frequency, a 20 kW AC power supply and ultrasonic irradiation (as an energy source) with a power of 500 W and a 40 kHz frequency. Cooling and stirring systems imposed a constant temperature (0°C)

during the U-SEO-P process to stabilize the electrochemical reactions for 180 s, in which with a Mg anode was immersed in an electrolyte composed of 8 g/L^{-1} K_3PO_4, 7 g/L^{-1} KOH, and 40 g/L^{-1} $C_2H_6O_2$ in 2 L of DI water (pH = 12). U-SEO-P is conventionally used to fabricate a porous MgO layer on a Mg substrate. After $Cu(NO_3)_2{\cdot}3H_2O$, $AgNO_3$, $Ni(NO_3)_2{\cdot}6H_2O$, $Fe(NO_3)_3{\cdot}9H_2O$, $Co(NO_3)_3{\cdot}6H_2O$, $Mn(NO_3)_2{\cdot}4H_2O$, or $Ru(NO_3)_3$ was added to a K_3PO_4-based electrolyte containing ethane-1,2-diol as the reducing agent, the metal ions were reduced to Cu, Ag, Ni, Fe, Co, Mn, or Ru, respectively.

Ultrasonic irradiation provides a cavitation effect that generates fine bubbles in the solution. The formation and bursting of bubbles produce local heating at the plasma discharge locations on the surface of the Mg substrate, creating weak spots in the barrier layer. The plasma sparks obtained under U-SEO-P were smaller and had a longer lifetime than those obtained under SEO-P (i.e., no ultrasonic irradiation). In this case, metal atoms could not spread across large distances, thus facilitating aggregation of the us-MEA-NPs on the porous MgO-P3000 surface due to the very small and very short-lived localized plasma discharges.

To understand the working mechanisms of U-SEO-P in depth, the cathode (work piece) was surrounded by a gas envelope. Electrical breakdown was observed in the vapor envelope around the oxide layer upon voltage application (several hundred volts), leading to ionization of the gas phase and the generation of soft plasma discharge in the near-cathode region. Moreover, the bubbles and NPs formed from reduction in the solution at extremely high temperatures were cooled by the electrolyte near the cathode surface, which accelerated the deposition and incorporation of metal elements (more details are provided in the Supporting Information).

The density of the plasma was greater in the presence of ultrasonic irradiation, that is, in U-SEO-P than in SEO-P. During the formation of us-MEA-NPs@MgO-P3000 in U-SEO-P, two concurrent processes occurred: (I) oxidation of the Mg alloy and (II) simultaneous decomposition and reduction of all metal salts in the electrolyte and oxidation of the Mg metal plate owing to the high voltage discharge, as summarized in Equations (4)–(7).

$$\mathrm{Mg} \rightarrow \mathrm{Mg}^{2+} + \mathrm{ne}^{-}. \tag{4}$$

$$\mathrm{Mg}^{2+} + \mathrm{H_2O} \rightarrow \mathrm{MgO} + 2\mathrm{H}^{+}. \tag{5}$$

$$2\mathrm{H}^{+} + 2\mathrm{e}^{-} \rightarrow \mathrm{H_2}\uparrow. \tag{6}$$

$$\mathrm{M}^{2+} + \mathrm{ne}^{-} \rightarrow \mathrm{M}^{0}. \tag{7}$$

The amount of ultrasonic irradiation transmitted to the electrolyte can be expressed by the acoustic energy density (W mL^{-1}), ultrasonic intensity (W cm^{-2}), cavitation intensity, or ultrasonic power (W). The ultrasonic power, acoustic energy density, and ultrasonic intensity are defined in Equations (8)–(10):

$$\text{Power (w)} = mC_p\left[\frac{dT}{dt}\right]_{t=0.} \tag{8}$$

$$\text{Ultrasonic intensity}\left(\text{w/cm}^2\right) = \frac{P}{A}. \tag{9}$$

$$\text{Acoustic energy density (W/mL)} = \frac{P}{V}. \tag{10}$$

where A is the area of the sample surface, D is the diameter of the ultrasonic probe, m is the mass, C_p is the specific heat capacity, V is the volume, and $\frac{dT}{dt}$ is the initial rate of temperature change during ultrasonic irradiation.

During the U-SEO-P process, the Mg anode was oxidized to yield a porous MgO-P3000 support, while the metal precursors in the solution that moved to the formed MgO-P3000 layer, were reduced under the high local temperature in ethane-1,2-diol to produce us-MEA-NPs. The us-MEA-NPs (nonvolatile liquid droplets) were instantaneously quenched on the support surface, forming CuAgNiFeCoRuMn-NPs on the MgO-P3000 support surface without phase separation, agglomeration, or element segregation. A unique embedded MgO-P3000 structure was formed, in which CuAgNiFeCoRuMn-NPs were firmly anchored on the surface of the porous MgO-P3000 support.

5.2 | Material characterization and catalytic reduction of nitroarene compounds

Full details of the characterization and catalytic reduction procedures are provided in the Supporting Information.

5.3 | Computational method

We used the ATAT code[48] to create a special quasirandom structure (SQS) of the CuAgNiFeNiCoRuMn high-entropy alloy (HEA) from a 5 × 2 × 1 supercell of the Ag (111) surface. The ATAT code uses a Monte Carlo strategy to find the best match for the paired correlation functions of the alloy of interest. Correlation functions capture the atomic arrangements in alloys and are therefore suitable

fingerprints when searching for crystal models. In the SQS (HEA), there were 112 atoms in the basic unit cell of the crystal structure. Ag, Fe, Ni, Cu, Ru, Co, and Mn had roughly equal proportions in the overall composition. The positions and cell parameters were optimized with the conjugate gradient method within cp2k with the Gaussian and plane wave (GPW) formalism[49] (quickstep method). The Perdew–Burke–Ernzerhof (PBE) exchange-correlation functional[50] was employed, as was the DZVP basis set in combination with the Goedecker–Teter–Hutter (GTH) pseudopotential.[51] The plane wave density cutoff was 400 Ry. The self-consistent field (SCF) convergence criterion was 1.0×10^{-6} Ha, and convergence was reached with a Broyden density mixing scheme. The DFT-D3 dispersion correction was used.[52] Partial DOSs were calculated for the optimized structures of both the CuAgNiFeCoRuMn and CuAgNiFeCoRhCoMn alloys and projected onto atomic orbitals.

Molecular dynamics (MD) simulations of hydrogen and hydrazine adsorption and activation on CuAgNiFeCoRuMn were performed based on ~20 nm NP models (329 atoms) obtained from the geometry-optimized periodic model. For efficiency and enhanced sampling, interatomic force calculations were based on the transferable tight-binding GFN-xTB scheme,[50–53] as implemented in cp2k.

5.4 | Thermodynamics calculations

ThermoCalc (v. 10) was used the SSOL7 database to calculate the mixing enthalpy (ΔH_{mix}), mixing entropy (ΔS_{mix}), and mixing Gibbs free energy (ΔG_{mix}). The calculations were performed for a liquid phase because the temperature caused by plasma discharge was high. To compare ΔH_{mix}, ΔS_{mix}, and ΔG_{mix} among systems with different numbers of components, equimolar systems were assumed.

AUTHOR CONTRIBUTIONS

Wail Al Zoubi: Conceptualization; methodology; investigation; formal analysis; writing, original draft; review and editing. **Stefano Leoni**: Formal analysis; conceptualization; methodology writing, original draft; review and editing. **Abdul Wahab Allaf** and **Bassem Assfour**: Formal analysis. **Jee-Hyun Kang**: Formal analysis; writing; original draft; review and editing. **Young Gun Ko**: Supervision; funding acquisition; visualization.

ACKNOWLEDGMENTS

This work was supported by the National Research Foundation (NRF) funded by Republic of Korea (No. NRF-2022R1A2C1004392). SI thanks ARCCA, Cardiff, for computing time, and we would like to thank Dr Nicola Seriani, ICTP for his valuable discussion.

CONFLICT OF INTEREST STATEMENT

The authors declare that they have no known competing financial interests or personal relationships that could have appeared to influence the work reported in this article.

DATA AVAILABILITY STATEMENT

The data that were used are confidential.

ORCID

Wail Al Zoubi https://orcid.org/0000-0003-4213-8481

REFERENCES

1. Fenton JL, Steimle BC, Schaak RE. Tunable intraparticle frameworks for creating complex heterostructured nanoparticle libraries. *Science*. 2018;360(6388):513-517.
2. Jouny M, Luc W, Jiao F. High-rate electroreduction of carbon monoxide to multi-carbon products. *Nature Catalysis*. 2018; 1(10):748-755.
3. Ding K, Cullen DA, Zhang L, et al. A general synthesis approach for supported bimetallic nanoparticles via surface inorganometallic chemistry. *Science*. 2018;362(6414):560-564.
4. Takahashi M, Koizumi H, Chun WJ, Kori M, Imaoka T, Yamamoto K. Finely controlled multimetallic nanocluster catalysts for solvent-free aerobic oxidation of hydrocarbons. *Sci Adv*. 2017;3(7):1700101.
5. Zhang B, Zheng X, Voznyy O, et al. Homogeneously dispersed multimetal oxygen-evolving catalysts. *Science*. 2016;352(6283): 333-337.
6. Chen PC, Liu X, Hedrick JL, et al. Polyelemental nanoparticles libraries. *Science*. 2016;352(6293):1565-1569.
7. Kwon SG, Krylova G, Phillips PJ, et al. Heterogeneous nucleation and shape transformation of multicomponent metallic nanostructures. *Nat Mater*. 2015;14(2):215-223.
8. Chen C, Kang Y, Huo Z, et al. Highly crystalline multimetallic nanoframes with three-dimensional electrocatalytic surfaces. *Science*. 2014;343(6177):1339-1343.
9. White RJ, Luque R, Budarin VL, Clark JH, Macquarrie DJ. Supported metal nanoparticles on porous materials. Methods and applications. *Chem Soc Rev*. 2009;38(2):481-494.
10. Hansen PL, Wagner JB, Helveg S, Rostrup-Nielsen JR, Clausen BS, Topsøe H. Atom-resolved imaging of dynamic shape changes in supported copper nanocrystals. *Science*. 2002; 295(5562):2053-2055.
11. Wong A, Liu Q, Griffin S, Nicholls A, Regalbuto JR. Synthesis of ultrasmall, homogeneously alloyed, bimetallic nanoparticles on silica supports. *Science*. 2017;358(6369):1427.
12. Gao S, Hao S, Huang Z, et al. Synthesis of high-entropy alloy nanoparticles on supports by the fastmoving bed pyrolysis. *Nat Commun*. 2020;11(1):2016.
13. Yao Y, Dong Q, Brozena A, et al. High-entropy nanoparticles: synthesis-structure-property relationships and data-driven discovery. *Science*. 2022;376(6589):151.

14. Kusada K, Mukoyoshi M, Wu D, Kitagawa H. Chemical synthesis, haracterization, and properties of multi-element nanoparticles. *Angew Chem Int Ed Engl*. 2022;61(25):202209616.
15. Prieto G, Zecevic J, Friedrich H, et al. Towards stable catalysts by controlling collective properties of supported metal nanoparticles. *Nat Mater*. 2013;12(1):34-39.
16. Al Zoubi W, Assfour B, Allaf AW, et al. Experimental and theortical investigation of high-entropy-alloy/support as a catalyst for reduction reactions. *J Energy Chem*. 2023;81: 132-142.
17. Yao Y, Huang Z, Xie P, et al. Carbothermal shock synthesis of high-entropy-alloy nanoparticles. *Science*. 2018;359(6383):1489-1494.
18. Chen F, Yao Y, Nie A, et al. High-temperature atomic mixing toward well-dispersed bimetallic electrocatalysts. *Adv Energy Mater*. 2018;8(25):1800466.
19. Minamihara H, Kusada K, Yamamoto T, et al. *J Am Chem Soc*. 2023;145(31):17136-17142.
20. Park I, Li ZY, Pisano AP, Williams RS. Selective surface functionalization of silicon nanowires via nanoscale joule heating. *Nano Lett*. 2007;7(10):3106-3111.
21. Liu Y, Ye C, Chen L, et al. High entropy-driven role of oxygen vacancies for water oxidation. *Adv Funct Mater*. 2024;34(25): 2314820.
22. Nyathi TM, York FN, Andrew PE, et al. Impact of nanoparticle−support interactions in Co_3O_4/Al_2O_3 catalysts for the preferential oxidation of carbon monoxide. *ACS Catal*. 2019;9(8): 7166-7178.
23. Al Zoubi W, Al Mahmud A, Hazmatulhaq F, et al. Origin of the synergistic effects of bimetallic nanoparticles coupled with a metal oxide heterostructure for accelerating catalytic performance. *SusMat*. 2024;4(3):216.
24. Chui M, Yang C, Hwang S, et al. Multi-princile elements intermetallic nanoparticles synthesizied via a disorderto-order transition. *Sci Adv*. 2022;8(4):4322.
25. Yao Y, Huang Z, Hughes LA, et al. Extreme mixing in nanoscale transition metal alloys. *Matter*. 2021;4(7):2340.
26. Minamihara H, Kusada K, Wu D, et al. Continuous-flow reactor synthesis for homogenous 1 nm-sized extremely small high-entropy alloy nanoparticles. *J Am Chem Soc*. 2022; 144(26):11525-11529.
27. Li T, Dong Q, Wu L, et al. Interface engineering between multi-elemental alloy nanoparticles and a carbon support toward stable catalysts. *Adv Mater*. 2022;34(9):2106436.
28. VandeVondele J, Krack M, Mohamed F, Parrinello M, Chassaing T, Hutter J. Quickstep: fast and accurate density functional calculations using a mixed Gaussian and plane waves approach. *Comput Phys Commun*. 2005;167(2): 103-128.
29. Sun J, Ren R, Yue H, et al. High-entropy perovskite oxide $BaCo_{0.2}Fe_{0.2}Zr_{0.2}Sn_{0.2}Pr_{0.2}O_{3-\delta}$ with triple conduction for the air electrode of reversible protonic ceramic cells. *Chin Chem Lett*. 2023;34(7):10776.
30. Wang H, Wang L, Lin D, et al. Strong metal-support interactions on gold nanoparticle catalysts achieved through Le Chatelier's principle. *Nature Catalys*. 2021;4(5):418-424.
31. Jung WB, Park H, Jang JS, et al. Polyelemental nanoparticles as catalysts for a Li-O_2 battery. *ACS Nano*. 2021;15(3):4235-4244.
32. Zhao K, Tang H, Qiao BT, Li L, Wang J. High activity of Au/γ-Fe_2O_3 for CO oxidation: effect of support crystal phase in catalyst design. *ACS Catal*. 2015;5(6):3528-3539.
33. Xu X, Guo Y, Bloom BP, et al. Elemental core level shift in high entropy alloy nanoparticles via x-ray photoelectron spectroscopy analysis and first-principles calculation. *ACS Nano*. 2020; 14(12):17704-17712.
34. Al Zoubi W, Kurnia PRA, Abukhadra KYG. Ecent expermental and theortical advances in the design and science of high-entropy alloy nanoparticles. *Nano Energy*. 2023;110:108362.
35. Zhang G, Tang F, Wang X, Wang L, Liu YN. Atomically dispersed Co-S-N active sites anchored on hierarchically porous carbon for efficient catalytic hydrogenation of nitro compounds. *ACS Catal*. 2022;12(10):5786-5794.
36. Zhang X, Li X, Zhang D, et al. Product selectivity in plasmonic photocatalysis for carbon dioxide hydrogenation. *Nat Commun*. 2017;8(1):14542.
37. Poulose AC, Zoppellaro G, Konidakis I, et al. Fast and selective reduction of nitroarenes under visible light with an earth-abundant plasmonic photocatalyst. *Nat Nanotechnol*. 2022; 17(5):485-492.
38. Wang T, Chen H, Yang Z, Liang J, Dai S. High-entropy perovskite fluorides: a new platform for oxygen evolution catalysis. *J Am Chem Soc*. 2020;142(10):4550-4554.
39. Ye YF, Wang Q, Lu J, Liu CT, Yang Y. High-entropy alloy: challenges and prospects. *Mater Today*. 2016;19(6):349-362.
40. Yeh JW, Chen SK, Lin SJ, et al. Nanostructured high-entropy alloys with multiple principal elements: novel alloy design concepts and outcomes. *Adv Eng Mater*. 2004;6(5):299-303.
41. Al Zoubi W, Allaf AW, Assfor B, Ko YG. Concurrent oxidation-reduction reactions in a single system using a low-plasma phenomenon: excellent catalytic perfromance and stabiliyy in the hydrogeation reaction. *ACS App Mater Interfaces*. 2022;14(5): 6740-6753.
42. Tang X, Thompson GB, Ma K, Weinberger CR. The role of entropy and enthalpy in high entropy carbides. *Comput Mater Sci*. 2022;210:111474.
43. Bao A, Gu Y, Zhang Y, et al. Boosting overall saline water splitting by constructing astrain-engineered high-entropy electrocatalyst. *Carbon Energy*. 2024;6(2):519.
44. Sun G, Liu D, Li M, et al. Atomic coordination structural dynamic evolution of single-atom Mo catalyst for promoting H_2 activation in slurry phase hydrocracking. *Sci Bull*. 2023; 68(5):503-515.
45. Sun G, Liu D, Shi H, et al. Oxygen-vacancy-induced built-in electric field across MoCo dual-atomic site catalyst for promoting hydrogen spillover in hydrocracking and hydrodesulfurization. *ACS Catal*. 2024;14(5):3208-3217.
46. Yang D, Tao S, Zhu H, et al. Construction of Rh-N_4 single atoms and Rh clusters dual-active sites for synergistic heterogeneous hydroformylation of olefins with ultra-high turnover frequency. *Chem Eng J*. 2024;479:147505.
47. Gao W, Liu S, Sun G, Zhang C, Pan Y. Single-atom catalysts for hydrogen activation. *Small*. 2023;19(26):2300956.
48. Perdew JP, Burke K, Wang Y. Generalized gradient approximation for the exchange-correlation hole of a many-electron system. *Phys Rev B*. 1996;54(23):16533-16539.
49. Goedecker S, Teter M, Hutter J. Separable dual-space Gaussian pseudopotentials. *Phys Rev B*. 1996;54(3):1703-1710.

50. Grimme S, Antony J, Ehrlich S, Krieg H. A consistent and accurate ab initio parametrization of density functional dispersion correction (DFT-D) for the 94 elements H-Pu. *J Chem Phys*. 2010;132:154104.
51. Qiao H, Saray MT, Wang X, et al. Scalable synthesis of high entropy alloy nanoparticles by microwave heating. *ACS Nano*. 2021;15(9):14928-14937.
52. Bannwarth C, Ehlert S, Grimme S. J GFN2-xTB-an accurate and broadly parametrized self-consistent tight-binding quantum chemical method with multipole electrostatics and density-dependent dispersion dontributions. *Chem Theory Comput*. 2019;15(3):1652-1671.
53. Al Zoubi W, Nashrah N, Putri RAK, et al. Strong dual-metal-support interactions induced by low-temperature plasma phenomenon. *Mater Today Nano*. 2022;18:100213.

SUPPORTING INFORMATION

Additional supporting information can be found online in the Supporting Information section at the end of this article.

How to cite this article: Al Zoubi W, Leoni S, Assfour B, Allaf AW, Kang J-H, Ko YG. Continuous synthesis of metal oxide-supported high-entropy alloy nanoparticles with remarkable durability and catalytic activity in the hydrogen reduction reaction. *InfoMat*. 2024;e12617. doi:10.1002/inf2.12617